Fracture effect on the hydro-mechanical behaviour of Callovo-Oxfordian claystone

Hao Wang, Yu-Jun Cui, Minh Ngoc Vu, Jean Talandier, Nathalie Conil

Fracture effect on the hydro-mechanical behaviour of Callovo-Oxfordian claystone

Hao Wang[1], Yu-Jun Cui[1], Minh Ngoc Vu[2], Jean Talandier[2], Nathalie Conil[2,*]

1: Ecole des Ponts ParisTech, Laboratoire Navier/CERMES, 6 et 8 avenue Blaise Pascal, 77455 Marne La Vallée cedex 2, France

2: Andra, R&D Department, 92290 Châtenay-Malabry, France

*: Now at Ineris, 60550 Verneuil-en-Halatte, France

Corresponding author

Dr Hao Wang

Ecole des Ponts ParisTech, Laboratoire Navier/CERMES, 6 – 8 av. Blaise Pascal, Cité Descartes, Champs-sur-Marne, 77455 Marne-la-Vallée cedex 2, France

Tel.: +33 767094216

E-mail address: hao.wang@enpc.fr

ABSTRACT

Excavation of the galleries for the geological disposal of radioactive waste can induce an excavation damaged zone (EDZ), which can have consequences on the long-term safety of the repository. In this study, intact Callovo-Oxfordian (COx) claystone taken from the Meuse/Haute-Marne Underground Research Laboratory in France was artificially fractured in different directions, and the hydro-mechanical behaviour was investigated by performing high pressure oedometer test and hydraulic conductivity test. Comparison between the fractured and intact COx samples allows identification of the effects of fracture in terms of swelling, compression, hydraulic conductivity and creep. It appears that the presence of fracture decreases the swelling strain and this phenomenon depends on the infiltration path and the orientation of fracture. In particular, the infiltration path affects the global swelling rate of fractured claystone. The self-sealing of fracture is mainly attributed to the swelling of COx claystone grains in the fracture zone. Lower compression coefficient a, higher compression index C_c* and higher secondary consolidation coefficient C_α are observed for the fractured claystone, indicating a higher compressibility and creep than the intact one. The compression and creep behaviours depend on both the orientation of fracture and the stress level. Comparison of hydraulic conductivities between fractured and intact claystone indicates that the hydraulic conductivity can be partially recovered due to the collapse of macro-pores in the filled fracture zone. This is also confirmed by analysing the evolution of consolidation coefficients c_v with stress. Beyond a stress level about 16 MPa, the fracture effect can be neglected, but the compressibility increases further due to grain breakage. Interestingly, this stress is close to the in-situ stress before excavation.

KEYWORDS: COx claystone; fracture; swelling; compression; creep; hydraulic conductivity.

INTRODUCTION

The French National Radioactive Waste Management Agency (Andra) is in charge of studying the disposal of high-level and intermediate-level long-lived waste (HLW and ILW-LL) in a deep geological repository (Cigéo project) which will be located at the border of the Meuse and Haute-Marne departments, nearly 300 km East of Paris. The host formation is the Callovo-Oxfordian (COx) claystone layer with ~ 150 m of thickness and located about 500 m in depth. This argillaceous rocks exhibit very favourable conditions for a repository of radioactive waste, as they generally have a very low hydraulic conductivity, small molecular diffusion and significant retention capacity for radionuclide. Andra is conducting a scientific and technological program, including in-situ experiments at the Meuse/Haute-Marne Underground Research Laboratory (MHM URL), which aims to demonstrate the feasibility of constructing and operating the Cigéo project (ANDRA, 2005). Among the in-situ experiments at MHM URL, field observation about the excavation induced damage zone (EDZ) has been made with particular attention. Indeed, a major concern related to the long term safety of the geological radioactive waste disposal is that the fractures within EDZ could create preferential pathways to the radionuclide migration. A conceptual model of EDZ around drifts excavated at the main level of MHM URL was proposed by Armand et al. (2014). The in-situ measurements indicated that the hydraulic conductivity of damaged COx claystone in the vicinity of drift was significantly higher than that far from the wall, due to the fractures in the EDZ (de la Vaissière et al., 2015; Armand et al., 2014). Moreover, the convergence of excavated galleries might be intensified by the presence of fractures within the EDZ (Armand et al., 2013). In other words, the rock formation with EDZ will produce more significant time-dependent deformation, impacting the long-term evolution of nuclear waste repository. As shown by Alonso et al. (2021), the creep strain of COx claystone mainly controls the stress increase within the gallery concrete liner (i.e. the design of the gallery liner).

A large number of laboratory tests were conducted on COx claystone to clarify the evolution of fractures upon wetting (Pham et al., 2007; Wan et al., 2013; Menaceur et al., 2016). It appears that the pre-existing fractures in COx claystone can be closed due to the swelling of the clay minerals (interstratified illite /smectites, illite, and kaolinite, etc.) (Yven et al., 2007; Menaceur, 2014). This phenomenon strongly depends on the applied stress, the clay fraction and the hydration level (Zhang, 2011 and 2013; Giot et al., 2019; Di Donna et al., 2019). Zhang (2009, 2011, 2013) explored the effect of fracture aperture on the permeability of COx claystone through gas and water permeability tests, with artificially created fractures. It was observed that the swelling of the clay matrix due to wetting induced clogging of fractures, leading to a significant decrease of gas and water permeabilities by several orders of magnitude. This indicates that the self-sealing property of COx claystone can result in partial recovery of its permeability with clogging of fractures. However, under free swelling conditions, micro-cracks occur inside the intact COx claystone due to swelling (Bornert et al. 2010; Wang et al. 2014; Menaceur et al. 2016). Besides, it is worth noting that the previous studies mainly focused on the swelling aspect of fractured COx claystone, less attention being paid to its compression behaviour.

Several studies were performed to investigate the volume change behaviour of intact COx claystone. Mohajerani et al. (2011) and Menaceur (2014) investigated the oedometer compression behaviour of intact COx claystone, showing that a high stress resulted in local pore collapse. Moreover, the damage-induced micro-cracks enhanced its swelling potential. Similar observations were observed on other swelling shales, which was interpreted by the damage of bonds by loading (Aversa et al., 1993; Carter et al., 2010). Besides, Chiarelli et al. (2003) investigated the isotropic compression behaviour of intact COx claystone at initially unsaturated state, and significant plastic volume change and anisotropic behaviour were observed, in agreement with the observations by Zhang et al. (2015, 2019). However, it

should be pointed out that previous studies only focused on the volume compression behaviour of intact claystone, few studies dealing with the volume change and creep behaviours of fractured COx claystone.

In this study, high pressure oedometer tests were carried out to investigate the effect of fracture on the hydro-mechanical behaviour of COx claystone. Two kinds of artificial fractured samples with different fracture directions (horizontal and vertical) were considered, together with an intact sample for the purpose of comparison. Besides, the hydraulic conductivity of COx claystone was measured in each loading step. The obtained results allowed the self-sealing characteristics and the effects of fracture on swelling, compression and creep behaviours of COx claystone to be clarified.

MATERIALS AND METHODS

Materials

The COx claystone used in this study was excavated at a depth of about -490 m, with a pore water pressure of 4.7 MPa and the in situ stresses of ~12.7 MPa in the vertical direction, ~12.7-14.8 MPa in the major horizontal stress direction, ~12.4 MPa in the minor horizontal stress direction (Wileveau et al., 2007). For the mineral composition, clay minerals account for 50-55%, including 30% illite, 15% kaolinite and chlorite and 55% interstratified illite\smectite. Besides, it also contains 3% pyrite, 20% iron oxides, 20%–25% tectosilicates of carbonates (Armand et al., 2013). The extracted COx claystone samples are preserved in T1 cell to keep the water content as in situ state and to minimize the decompression due to unloading from in situ stress (Conil et al., 2018). In this study, a COx core from T1 cell EST57180 was used. The physical parameters of this core were determined and presented in Table 1. Decagon WP4 dew point tensiometer was used to measure the initial total suction. Small pieces were cut to measure the water content by oven drying at 105 °C. The porosity

123 (void ratio) and degree of saturation were determined by measuring the volume (see
124 Menaceur et al. (2016) for more details). Then, the dry density can be calculated.

125 **Sample preparation**

126 For the real fractures induced under the in situ conditions, they are quite complex (e.g.
127 fracture size, number and direction), as reported by Armand et al. (2014). The fractures are
128 classified into two types: shear fractures and unloading tensile fractures, based on the
129 observations on drill cores. The shear fractures are generally oriented at an angle with respect
130 to the drift wall, while most tensile fractures are perpendicular to the corresponding bedding
131 plane in the vicinity of drift wall. In this context, it is very difficult to identify the effect of
132 fractures on the hydro-mechanical behaviour of COx claystone. To simplify the problem, only
133 a well-defined single horizontal/vertical fracture with respect to the bedding direction is
134 considered in this study. For the preparation of fractured COx claystone samples, a COx
135 cylinder with diameter of 38 mm was first drilled along the direction perpendicular to the
136 bedding plane. A diamond sawing machine was used to cut the cylinder to oedometer samples
137 of 10 mm height. The preparation process is shown in Fig. 1. To acquire fractured samples,
138 the intact sample was artificially cut into two parts in two directions - parallel (horizontal
139 fracture) and perpendicular (vertical fracture) to the bedding plane as shown in Fig. 2. An
140 intact sample was also used for comparison. For the horizontally fractured samples, the
141 average width of a horizontal fracture depends on the roughness of the contact interface of the
142 two disks after sand paper polishing. Each disk has a diameter of 38 mm and a height of 5 mm.
143 The objective of polishing the interface was to well define the fracture width. The horizontal
144 fracture thickness was determined as the difference between the total height of the two
145 stacked disks after placed in the oedometer cell and the sum of the heights of the two separate
146 disks. For the vertically fractured samples, the vertical fracture thickness was obtained by
147 measuring the difference between the diameter in the direction perpendicular to the vertical

148 fracture and the initial one before cutting. For the control of vertical fracture size, a thin metal
149 plate was used to separate the two parts after the sample was placed in the oedometer cell.

150 **Experimental methods**

151 High pressure oedometer was used and synthetic water was adopted with the same chemical
152 composition as the site water, as shown in Table 2. The in situ COx claystone in the fractured
153 zone is unsaturated due to the ventilation, but will be saturated after closure by the in situ
154 water from the surrounding host formation. In order to simulate the swelling behaviour of
155 fractured COx claystone in the fractured zones, two cases were considered: case 1 - the
156 sample was wrapped with filter paper at the lateral surface to simulate the underground water
157 directly flowing into the fractures (tests TH-1 and TV-1); case 2 - without filter paper at the
158 lateral surface to simulate the underground water infiltrating into fracture through intact COx
159 claystone (tests TH-2 and TV-2). Test TI was performed on the intact sample without filter
160 paper at the lateral surface. The programs for the five tests are detailed in Table 3. It can be
161 observed that different fracture openings were used for horizontal (0.1 mm) and vertical (0.3
162 mm) fractures. This choice was made to ensure that all samples had the same initial global
163 void ratio. Note that the initial global void ratio considered all the void including the facture
164 and the void inside the disks. In addition, based on the experimental evidence by Giot et al.
165 (2019) and Di Donna et al. (2019), the selection of the fracture sizes in this study can ensure
166 the fractures be totally closed by the swelling of clay minerals due to hydration.

167 After the sample was installed into the oedometer cell, synthetic water was injected from
168 the bottom under a low vertical stress of 0.05 MPa to ensure the good contact. After the
169 stabilization of vertical swelling strain according to ASTM-D4546 (2021), step loading up to
170 64 MPa was applied. At each loading step, the hydraulic conductivity (k) was measured in the
171 vertical direction with a pressure-volume controller, as shown in Fig. 3.

Actually, considering the fracture effect, significantly large pores exist in the closed fracture zone due to the swelling of clay minerals, as reported by Zhang (2011, 2013). Thus, the samples cannot be regarded as homogeneous accounting for the presence of obvious dual porosity (large pores in fractured zone and small pores in intact zone). Strictly speaking, it is not suitable to analyze the consolidation behaviour of fractured COx claystone using the Terzaghi consolidation theory due to the heterogeneity of samples. However, the direct application of this theory seems to be the easiest way to evidence the effect of fractures on permeability and compressibility. Therefore, in this study, the simplified one-dimensional consolidation equation is still adopted to calculate the hydraulic conductivity and compression coefficient, as shown in Eq. (1) (Terzaghi et al., 1996):

$$c_v \frac{\partial^2 u_e}{\partial z^2} = \frac{\partial u_e}{\partial t} \tag{1}$$

where u_e is the excess pore water pressure, σ_z is the total vertical stress, t is the time, and c_v is the consolidation coefficient.

c_v can be calculated with Eq. (2):

$$c_v = \frac{k(1+e)}{\gamma_w a_v} \tag{2}$$

where k is the hydraulic conductivity, a_v is the compression coefficient, e is the corresponded void ratio under each stress and γ_w is the water unit weight. The compression coefficient a_v is the ratio between the decrement of e and the increment of σ_v. $a_{v,n}$ at the loading step n can be calculated as following:

$$a_{v,n} = \frac{e_n - e_{n-1}}{\sigma_{v,n} - \sigma_{v,n-1}} \tag{3}$$

where e_n and e_{n-1} are the void ratios at the loading step n and the last one, respectively; $\sigma_{v,n}$ and $\sigma_{v,n-1}$ are the corresponding vertical stresses.

194 In addition, based on the time-deformation curve under each vertical stress in oedometer
195 test, the consolidation coefficient c_v can also be determined by Eq. (4) (ASTM-D2435, 2020).
196 In this study, Eq. (4) is obtained with the Log of Time Method.

197 $$c_v = \frac{T_{50} H_{D_{50}}^2}{t_{50}} \quad (4)$$

198 where $T_{50} = 0.197$, t_{50} is the time corresponding to 50 % of the primary consolidation, H_{D50}
199 is the length of the drainage path at 50 % of primary consolidation. Thus, the global vertical
200 hydraulic conductivity (k) can be calculated by combining Eqs. (2) and (4), as shown in Eq.
201 (5).

202 $$k = \frac{T_{50} H_{D_{50}}^2}{t_{50}} \times \frac{\gamma_w a_v}{1+e} \quad (5)$$

203 Moreover, Considering the gradual yielding of COx claystone with stress, the step
204 compression index C_c* is determined to study the variation of compressibility with stress, as
205 recommended by Deng et al. (2012) and Wang et al. (2021). Based on the time-void ratio
206 curve, the secondary consolidation coefficient C_α is determined to analyze the creep behavior
207 (ASTM-D2435, 2020).

208 **RESULTS AND DISCUSSIONS**

209 **Swelling behaviour**

210 Upon hydration with synthetic water injection under the initial stress, the samples swelled in
211 the two cases (with and without filter paper). Fig. 4 shows the evolution of vertical swelling
212 strains with time. Three stages can be identified: initial swell, primary swell and secondary
213 swell, as recommended by Rao et al. (2006) and ASTM-D4546 (2021). The vertical swelling
214 strain increased slowly with time at the beginning, then increased quickly, finally increased
215 progressively. At the end of the swelling process, test TH-1 exhibited a higher axial strain than
216 test TV-1 (3.49 % against 3.06 %) in case 1, while the vertical strains of tests with fractures

(TH-2: 3.19 % and TV-2: 3.38 %) are closer in case 2. The vertical strains in both cases are smaller than that of test TI (3.54 %).

Fig. 5 shows the evolution of vertical swelling strain rate with time, which is defined as the difference of swelling strain at time interval in log scale. It is found that the vertical swelling strain rates of all tests increased with time at the beginning, then reached the maximum, finally decreased steadily. As presented in Fig. 5a, the vertical swelling strain rates of test TH-1 in the initial swell and secondary swell stages were slightly lower than that of test TV-1, while much larger in the primary swell stage. However, in the case without filter paper (case 2, tests TH-2, TV-2 and TI), a similar vertical swelling strain rate was observed in the primary swell stage (Fig. 5b). In the initial swell stage, TV-2 has a larger swelling rate than TH-2 and TI. Nevertheless, test TI has a larger swelling rate than tests TH-2 and TV-2 in the secondary swell stage.

Fig. 6 can be used to explain the observed swelling phenomena. As the injection direction was vertical synthetic water went into the vertical fracture more easily even in the case with filter paper. Thus, the samples with vertical fracture swelled more quickly in the initial swell stage, as shown in Fig. 5. In case 1 with filter paper, after water entered the horizontal fracture via the filter paper, the hydration rate of test TH-1 speeded up because of the shorter infiltration path compared to test TV-1, resulting in a higher vertical swelling strain rate in the primary swell stage (Fig. 5a). In addition, at the end of the tests, the higher final swelling strain and lower strain rate of test TH-1 lead to a swelling strain closer to that of test TV-1. This can be explained by their similar global initial void ratios or dry densities. By contrast, in case 2 without filter paper, as tests TH-2 and TI have the same infiltration path, similar vertical swelling strains (Fig. 4b) and strain rates (Fig. 5b) were observed in the initial and primary swelling stages. It can thus be inferred that the swelling of fractured claystone depends on the infiltration path and the direction of the initial fracture.

242 Due to the effect of swelling, the fractures can be closed. This corresponds to the self-
243 sealing property as reported by Zhang (2011, 2013). The self-sealing in COx claystone is
244 mainly induced by the swollen clay minerals, as demonstrated by Giot et al. (2019) and Di
245 Donna et al. (2019) through 3D tomography observations. Due to self-sealing, the hydraulic
246 conductivity decreases gradually, as observed by Giot et al. (2019). From a hydro-mechanical
247 point of view, it appears that the self-sealing process can be divided into three stages (van
248 Geet et al., 2008; Zhang, 2011; de la Vaissière et al., 2015): (i) fracture closure - the swelling
249 of claystone near the fracture surface induces fracture closure with the expansion of clay
250 minerals; (ii) fracture clogging - the claystone grains disaggregate and clog the fracture zone;
251 (iii) homogenization - the macro-pores between the disaggregated claystone grains collapse
252 by the further swelling of claystone farther from the fracture zone.

253 **Compression, hydraulic conductivity and creep**

254 All compression curves are reported in Fig. 7 and Fig. 8a for case 1 and case 2, respectively,
255 in terms of global void ratio (including the filled fracture). Fig. 7 shows that with increasing
256 vertical stress, the void ratios of test TH-1 become smaller than that of test TV-1, indicating
257 that the compressibility of the sample with a horizontal fracture is higher than that with
258 vertical fracture. This confirms the dependency of the compression behaviour on the fracture
259 orientation. A similar phenomenon is observed in Fig. 8a. The yield stress (0.45 MPa) of test
260 TH-1 is smaller than that of test TV-1 (0.65 MPa). The similar phenomenon is observed while
261 comparing TH-2 and TV-2: the yield stress of test TH-2 (0.48 MPa) is smaller than that of
262 TV-2 (0.71 MPa). By contrast, test TI exhibits a significantly higher yield stress (1.08 MPa).
263 Besides, the curve of test TI becomes closer to that of test TH-2 in the high stress range, as
264 shown in Fig. 8a. It appears from these results that: (i) the filled fracture zone due to swelling
265 is a weak zone, resulting in a higher compressibility of the fractured sample; (ii) the increase
266 of stress can induce the collapse of the macro-pores in the filled fracture zone, enabling the

compression curve to gradually approach the intact one. Note that this macro-pore collapse effect was also reported by Zhang (2011, 2013). In addition, an increase of the slopes of compression curves is observed after 16 MPa (Fig. 7 and Fig. 8a), indicating an increase in compressibility. Interestingly, the oedometer tests conducted by Mohajerani, et al. (2011) and Menaceur (2014) on intact COx claystone also showed a similar compression phenomenon - with the increase of vertical stress, the slope of the compression curve increases continuously even under higher stress, up to 100 MPa. This is different from the observations on common clays - the slope first increases, then decreases (Mesri and Godlewski, 1977). Wang et al. (2021) reported that this increase in compressibility is due to the breakage of calcite and quartz in claystone. As mentioned before, calcite and quartz grains account for around 50% of the mineral composition of COx claystone. Wang (2012) observed that the calcite and quartz grains in COx claystone can be crushed under uniaxial compression.

The measured vertical hydraulic conductivity (k) is shown in Fig. 8b. By referring to the compression curves shown in Fig. 8a, it is found that the k of test TV-2 slightly decreases with loading before the yield stress, then decreases significantly. This is closely related to the volume change of the sample. A similar phenomenon was observed by Zhang (2011, 2013). Blackwell et al. (1990) highlighted that the hydraulic conductivity of clayey soils is significantly related to the macro-porosity. In this sense, it can be inferred that the measured k of test TV-2 is controlled by the large pores in the filled fracture zone. For test TH-2, the measured k is governed by the small pores in the intact part, which can be deduced from the comparison between tests TH-2 and TI in Fig. 8b. This is correlated to the direction of the measured k (vertical) with respect to the direction of fracture (horizontal). Note that intact part means the zone without fracture inside the sample before the test. The stress 0.25 MPa (Fig. 8b) can be regarded as the yield point of intact part in test TV-2. Interestingly, this stress corresponds to the yield stress identified in Fig. 8a. After around 16 MPa, the k of TV-2

292 decreases steadily and is comparable with that of test TI, indicating that the hydraulic
293 conductivity of the fractured sample is “recovered” to the intact one (Fig. 8b). By contrast,
294 due to the steady decrease of the porosity of the intact part, test TH-2 displays a gradual
295 decrease of *k*, as test TI.

296 To further estimate the hydraulic conductivity of COx claystone, the hydraulic conductivity
297 was also determined by back-analyzing the oedometer test results based on the consolidation
298 theory (ASTM-D2435, 2020). All values obtained (*k*-calculation) are summarized and
299 presented against vertical effective stress and void ratio in Fig. 9. With the increase of vertical
300 effective stress, all hydraulic conductivities exhibit a similar decreasing tendency (Fig. 9a).
301 Fig. 9b shows that small changes of void ratio can lead to a significant reduction of hydraulic
302 conductivity, indicating the strong dependencies on volume change. For test TI, the measured
303 *k* is similar to the calculated one at a low vertical stress or a large void ratio, while
304 significantly larger than the latter at a high vertical stress or a small void ratio. This is
305 attributed to the effect of physico-chemical interaction between bound water and clay particle
306 in the low-compressibility zone of soils, as reported by Mesri et al. (1994a) and Su et al.
307 (2020). The similar phenomenon is observed on test TH-2. However, the measured *k* in test
308 TV-2 is obviously larger than the calculated one at a low vertical stress or a large void ratio,
309 showing the effect of infiltration path (infiltration direction parallel to the fracture), as shown
310 in Fig. 6. Besides, at a same vertical stress or void ratio, the measured and calculated *k* in test
311 TV-2 both are larger than those of the other two tests even after the closure of fracture under
312 high stress, which indicates that the large pores in the filled fracture zone indeed intensify the
313 hydraulic conductivity. Favero et al. (2016) and Crisci et al. (2019) made the similar
314 observations on Opalinus clay shale, pointing out that the hydraulic conductivity is
315 significantly affected by the larger pores and can be enhanced by the presence of fractures.

316 Fig. 10 depicts the evolutions of compression coefficient a_v and consolidation coefficient
317 c_v, which are determined by Eqs. (3) and (4), respectively. a_v and c_v both decrease rapidly in
318 low stress range with the increase of vertical stress for tests TH-2, TV-2 and TI. Beyond
319 16 MPa, the compression coefficients a_v of three tests change little and exhibit the same
320 decreasing tendency (Fig. 10a). This further confirms that the fracture effect on
321 compressibility is negligible. Besides, the values of consolidation coefficient c_v also tend to
322 stabilize (Fig. 10b). Because the void ratios change little (Δe less than 0.1) in Fig. 8a, while
323 the hydraulic conductivities change by several orders of magnitude in Fig. 9b, it can be
324 inferred that c_v is rather governed by the variation of hydraulic conductivity. Thus, the higher
325 c_v of test TV-2 as compared to those of tests TH-2 and TI (Fig. 10b) also verifies the
326 observations from Fig. 9. Compared to test TI, test TV-2 has a hydraulic conductivity indeed
327 intensified by the macro-pores in the filled fracture zone, while TH-2 shows the negligible
328 effect of the filled fracture zone. This confirms the dependency of hydraulic conductivity on
329 the orientation of fractures.

330 To further analyse the effect of fracture on compression and creep, two parameters C_c* and
331 C_α are calculated. The calculation method is shown in Fig. 11. Fig. 12 shows that with the
332 increase of stress in case 1, both C_c* and C_α increase first, then change little, finally increase
333 significantly. The C_α and C_c* of test TH-1 are slightly higher than those of test TV-1, showing
334 the effect of fracture orientation. This also suggests that although the fracture was healed up
335 by swelling, the filled fracture zone is mechanically still a weak zone, characterised by higher
336 compressibility and a larger creep. The C_c* and C_α in Fig. 12 are replotted with respect to the
337 fracture orientation in Fig. 13. It is observed that both C_α and C_c* show a three-stage
338 relationship. C_α and C_c* almost increase linearly with stress in the lower (zone I) and higher
339 stress (zone III) ranges, but change little in the mid-range (zone II). The stress (1 MPa) for
340 TH-1 corresponding to the dividing point between zone I and zone II is lower than that (4

MPa) for TV-1. The stresses (around 16 MPa) corresponding to the dividing point between zone II and zone III are almost the same, which is consistent with the observations made on the compression curves in Fig. 7 and Fig. 8a.

Fig. 14 depicts the evolutions of C_c* and C_α of tests TH-2 and TV-2 in case 2, together with that of TI. A negligible effect of infiltration paths is observed – the evolutions are similar for tests TH-2 and TV-2. It is worth noting that before 16 MPa, the C_α and C_c* of tests TH-2 and TV-2 are significantly higher than those of test TI, showing a higher compressibility and a higher creep. This is consistent with the compression curves shown in Fig. 8a. Besides, for test TI, C_c* and C_α exhibit a continuously increasing tendency, suggesting that the compressibility and creep of COx claystone are stress-dependent. This phenomenon is quite uncommon because C_c* and C_α increase generally with the increase of stress in the low stress range, while keeping almost constant in the high stress range (Mesri and Godlewski, 1977; Lambe and Whitman, 1979; Favero et al., 2016). This is to be attributed to the breakage of calcite and quartz grains, as mentioned previously (Wang et al., 2021).

A conceptual model can be proposed to describe the evolutions of C_c* and C_α with stress (Fig. 15). Two key points, transitional and threshold points, are defined. There are significant differences (ΔC_c* and ΔC_α) between the fractured sample and the intact sample before the threshold point. Before the transitional point, ΔC_c* and ΔC_α increase with increasing stress, then reach the maximum values at the transitional stress, suggesting that the effect of weak fracture zone to the compressibility and creep reach the maximum. The corresponding transitional stress depends on the fracture orientation, as observed in Fig. 13. After the transitional point, ΔC_c* and ΔC_α decrease with increasing stress. At the threshold point (around 16 MPa), ΔC_c* and ΔC_α are close to zero, suggesting that the influence of fracture becomes negligible. After that, the fractured and intact samples exhibit similar C_c* and C_α, suggesting that the compression and creep properties of fractured claystone are almost

366 recovered. Note that the threshold stress 16 MPa is close to the in situ stresses (12 - 16 MPa)
367 (Wileveau et al., 2007). Beyond this stress, the stable structure formed by the grain inclusions
368 (quartz and calcite, etc.) under the in situ stress state was significantly disturbed, giving rise to
369 a drastic change of compressibility. This indicates the effect of stress history on the
370 compression behaviour of COx claystone.

371 Fig. 16 shows the relationship between C_α and C_c* for all the tests. It is almost linear for the
372 intact claystone with a slope of 0.0358. This is consistent with the observations (C_α/ C_c* =
373 0.03 ± 0.01) on shale and mudstone (Mitchell and Soga, 2005; Deng et al., 2012).
374 Interestingly, for the fractured claystone, C_α is significantly larger than that predicted by a
375 linear relationship before C_c* = 0.045 which corresponds to 16 MPa of stress (i.e. threshold
376 point) in Fig. 15. After that, the fractured and intact samples show similar C_α/C_c* values,
377 indicating a negligible effect of fracture in the high stress range. Mesri et al. (1994b) reported
378 that softer soils have a larger C_α/C_c* value. It can be thus inferred that the larger C_α results
379 from the weaker mechanical property of the filled fracture zone.

380 **CONCLUSIONS**

381 In this study, oedometer tests were conducted on fractured and intact COx claystone samples,
382 aiming at investigating the effects of fracture on its hydro-mechanical behaviour in terms of
383 swelling, compression, creep and hydraulic conductivity. The obtained results allow the
384 following conclusions to be drawn:

385 The presence of fracture decreases the swelling strain of the claystone sample and this
386 phenomenon depends on the infiltration path and the orientation of fracture. In particular, the
387 infiltration path affects the global swelling rate of fractured claystone. The self-sealing of
388 fracture is mainly attributed to the swelling and clogging of COx claystone grains in the
389 fracture zone.

390 Due to the weaker mechanical properties of the filled fracture zone, lower compression
391 coefficient a_v, higher compression index C_c* and higher secondary consolidation coefficient
392 C_α are observed for the fractured claystone, defining higher compressibility and more
393 significant creep than the intact one. Besides, comparing the results of tests on fractured
394 samples with different fracture directions, it is found that the test on vertically fractured
395 sample presents a larger yield stress and consolidation coefficient, as well as a smaller
396 compression index and secondary consolidation coefficient. This indicates the compression
397 and creep behaviours depend on the orientation of fracture and the stress level. Comparison of
398 hydraulic conductivities between the fractured and intact claystone samples indicates that the
399 hydraulic conductivity can be partially recovered due to the collapse of macro-pores in the
400 filled fracture zone. This is also confirmed by analysing the evolution of consolidation
401 coefficients c_v with stress.

402 These findings clearly show the effect of fracture on the swelling, compression, creep and
403 hydraulic conductivity of COx claystone. An interesting behaviour has been highlighted
404 concerning the stress level. Beyond 16 MPa, the fracture effect can be neglected, but the
405 compressibility increases further due to grain breakage. Fracture accelerate the creep strain,
406 confirming the field measurement in the MHM URL. This fracture-dependent creep
407 behaviour is a key issue in the design of the gallery concrete liner to ensure its stability during
408 the operational phase of the geological disposal.

409 **ACKNOWLEDGEMENTS**

410 The supports from China Scholarship Council (CSC), Ecole des Ponts ParisTech and French
411 National Radioactive Waste Management Agency (Andra) are gratefully acknowledged.

412 **REFERENCES**

Alonso, M., Vu, M.N., Vaunat, J., Armand, G., Gens, A., Plua, C., 2021. Effect of thermo-hydro-mechanical coupling on the evolution of stress in the concrete liner of an underground drift in the Cigéo project. In *IOP Conference Series: Earth and Environmental Science* (Vol. 833, No. 1, p. 012200). IOP Publishing.

ANDRA, 2005. Dossier Argiles, Référentiel du site Meuse/Haute Marne.

ASTM, D2435 / D2435M-11., 2020. Standard Test Method for One-Dimensional Consolidation Properties of Soils. ASTM International.

ASTM, D4546-21., 2021. Standard test methods for one-dimensional swell or collapse of soils. ASTM Book of Standard Specifications, Designation: D, 4546-14.

Armand, G., Noiret, A., Zghondi, J., Seyedi, D. M., 2013. Short-and long-term behaviors of drifts in the Callovo-Oxfordian claystone at the Meuse/Haute-Marne Underground Research Laboratory. *J. Rock Mech. Geotech. Eng.* 5, 221-230.

Armand, G., Leveau, F., Nussbaum, C., de La Vaissiere, R., Noiret, A., Jaeggi, D., Landrein P., Righini, C., 2014. Geometry and properties of the excavation-induced fractures at the Meuse/Haute-Marne URL drifts. *Rock Mech. Rock. Eng.* 47, 21-41.

Aversa, S., Evangelista, A., Leroueil, S., Picarelli, L., 1993. Some aspects of the mechanical behaviour of structured soils and soft rocks. In: Anagnostopoulos, editor. Geotechnical engineering of hard soils–soft rocks. Rotterdam: Balkema.

Blackwell, P. S., Ringrose-Voase, A. J., Jayawardane, N. S., Olsson, K. A., McKenzie, D. C., Mason, W. K., 1990. The use of air-filled porosity and intrinsic permeability to air to characterize structure of macropore space and saturated hydraulic conductivity of clay soils. *Journal of Soil Science* 41, 215-228.

435 Bornert, M., Vales, F., Gharbi, H., Nguyen Minh, D., 2010. Multiscale full-field strain
436 measurements for micromechanical investigations of the hydromechanical behaviour of
437 clayey rocks. *Strain* 46, 33-46.

438 Carter, TG., Castro, SO., Carvalho, J.L., Hattersley, D., Wood, K., Barone, F.S., et al., 2010.
439 Tunnelling issues with Chilean tertiary volcaniclastic rocks. Mir conference; Problemi di
440 stabilita nelle opere geotecniche. Capitolo 11, Torino.

441 Chiarelli, A. S., Shao, J. F., Hoteit, N., 2003. Modeling of elastoplastic damage behavior of a
442 claystone. *International Journal of plasticity* 19, 23-45.

443 Conil, N., Talandier, J., Djizanne, H., de La Vaissière, R., Righini-Waz, C., Auvray, C.,
444 Morlot, C., Armand, G., 2018. How rock samples can be representative of in situ
445 condition: A case study of Callovo-Oxfordian claystones. *J. Rock Mech. Geotech. Eng.*
446 10, 613-623.

447 Crisci, E., Ferrari, A., Giger, S. B., Laloui, L., 2019. Hydro-mechanical behaviour of shallow
448 Opalinus Clay shale. *Eng. Geol.* 251, 214-227.

449 de La Vaissière, R., Armand, G., Talandier, J., 2015. Gas and water flow in an excavation-
450 induced fracture network around an underground drift: a case study for a radioactive
451 waste repository in clay rock. *Journal of Hydrology* 521, 141-156.

452 Deng, Y. F., Cui, Y. J., Tang, A. M., Li, X. L., Sillen, X., 2012. An experimental study on the
453 secondary deformation of Boom clay. *Appl Clay Sci.* 59, 19-25.

454 Di Donna, A., Charrier, P., Salager, S., Bésuelle, P., 2019. Self-sealing capacity of argillite
455 samples. In E3S Web of Conferences (Vol. 92, p. 03005). EDP Sciences.

456 Favero, V., Ferrari, A., Laloui, L., 2016. On the hydro-mechanical behaviour of remoulded
457 and natural Opalinus Clay shale. *Eng. Geol.* 208, 128-135.

458 Giot, R., Auvray, C., Talandier, J., 2019. Self-sealing of claystone under X-ray
459 nanotomography. Geological Society, London, Special Publications, 482(1), 213-223.

460 Lambe, T.W., Whitman, R.V., 1979. *Soil Mechanics*. Wiley and Sons.

461 Mesri, G., Godlewski, P. M., 1977. Time and stress-compressibility interrelationship. *ASCE J*
462 *Geotech Eng Div.* 103, 417-430.

463 Mesri, G., Feng, T. W., Ali, S., Hayat, T. M., 1994a. Permeability characteristics of soft clays.
464 In *International conference on soil mechanics and foundation engineering*, 187-192.

465 Mesri, G., Kwan, L.D.O., Feng, W.T., 1994b. Settlement of embankment on soft clays. *Proc.*
466 *of Settlement 94.* ASCE Geotechnical Special Publication 40, 8–56.

467 Mitchell, J. K., Soga, K., 2005. Fundamentals of soil behavior (Vol. 3). Hoboken, NJ: John
468 Wiley & Sons.

469 Mohajerani, M., Delage, P., Monfared, M., Tang, A. M., Sulem, J., Gatmiri, B., 2011.
470 Oedometric compression and swelling behaviour of the Callovo-Oxfordian argillite. *Int.*
471 *J. Rock Mech. Min. Sci.* 48, 606-615.

472 Menaceur, H., 2014. Comportement thermo-hydro-mécanique et microstructure de l'argilite
473 du Callovo-Oxfordien. *PhD thesis*, Université Paris-Est, Paris.

474 Menaceur, H., Delage, P., Tang, A. M., Talandier, J., 2016. The status of water in swelling
475 shales: an insight from the water retention properties of the Callovo-Oxfordian claystone.
476 *Rock Mech. Rock. Eng.* 49, 4571-4586.

477 Pham, Q. T., Vales, F., Malinsky, L., Minh, D. N., Gharbi, H., 2007. Effects of desaturation–
478 resaturation on mudstone. *Phys. Chem. Earth.* 32, 646-655.

479 Rao, S. M., Thyagaraj, T., Thomas, H. R., 2006. Swelling of compacted clay under osmotic
480 gradients. *Géotechnique* 56, 707-713.

Su, W., Cui, Y. J., Zhang, F., Ye, W., 2020. Revisiting the methods of determining hydraulic conductivity of saturated expansive clays in low-compressibility zone. *J. Rock Mech. Geotech. Eng.* 12, 1131-1136.

Terzaghi, K., Peck, R. B., Mesri, G., 1996. Soil mechanics in engineering practice. John Wiley & Sons.

van Geet, M., Bastiaens, W., Ortiz, L., 2008. Self-sealing capacity of argillaceous rocks: review of laboratory results obtained from the SELFRAC project. *Phys. Chem. Earth.* 33, S396-S406.

Wan, M., Delage, P., Tang, A. M., Talandier, J., 2013. Water retention properties of the Callovo-Oxfordian claystone. *Int. J. Rock Mech. Min. Sci.* 64, 96-104.

Wang, L., 2012. Micromechanical experimental investigation and modelling of strain and damage of argillaceous rocks under combined hydric and mechanical loads. *Doctoral dissertation*, Palaiseau, Ecole polytechnique.

Wang, L. L., Bornert, M., Héripré, E., Yang, D. S., Chanchole, S., 2014. Irreversible deformation and damage in argillaceous rocks induced by wetting/drying. *Journal of Applied Geophysics* 107, 108-118.

Wang, H., Cui, Y. J., Zhang, F., Liu, J., 2021. Effect of grain breakage on the compressibility of soils. *Acta Geotechnica*, 1-10. https://doi.org/10.1007/s11440-021-01256-z

Wileveau, Y., Cornet, F. H., Desroches, J., Blumling, P. 2007. Complete in situ stress determination in an argillite sedimentary formation. *Phys. Chem. Earth.* 32, 866-878.

Yven, B., Sammartino, S., Geraud, Y., Homand, F., Villieras, F., 2007. Mineralogy, texture and porosity of Callovo-Oxfordian argillites of the Meuse/Haute-Marne region (eastern Paris Basin). *Mémoires de la Société géologique de France*, 178(1), 73-90.

Zhang CL., 2009. Self-sealing of fractures in argillites under repository conditions. In: International conference and workshop in the framework of the EC TIMODAZ and THERESA projects.

Zhang, C. L., 2011. Experimental evidence for self-sealing of fractures in claystone. *Phys. Chem. Earth.* 36, 1972-1980.

Zhang, C. L., 2013. Sealing of fractures in claystone. *J. Rock Mech. Geotech. Eng.* 5, 214-220.

Zhang, C. L., Armand, G., Conil, N., 2015. Investigation on the anisotropic mechanical behavior of the Callovo-Oxfordian clay rock. Final report.

Zhang, C. L., Armand, G., Conil, N., Laurich, B., 2019. Investigation on anisotropy of mechanical properties of Callovo-Oxfordian claystone. *Eng. Geol.* 251, 128-145.

515 **LIST OF TABLES**

516 Table 1. Initial characteristics of COx claystone core

517 Table 2. Chemical composition of the synthetic water

518 Table 3. Test programme

519

520 **LIST OF FIGURES**

521 Fig. 1. Schematic representation of the preparation of intact oedometer sample.

522 Fig. 2. Schematic diagram of Oedometer samples with horizontally (TH) and vertically (TV)
523 fractured directions and intact sample (TI) (dotted line: fracture).

524 Fig. 3. High pressure oedometer connected to a pressure-volume controller.

525 Fig. 4. Vertical swelling strain versus time; (a) Case 1; (b) Case 2 and test TI.

526 Fig. 5. Vertical swelling strain rate ($\Delta\varepsilon/\Delta\log t$) versus time: (a) Case 1; (b) Case 2 and test TI.

527 Fig. 6. Schematic view of water infiltration and soil swelling: (a) Case 1; (b) Case 2 and test
528 TI.

529 Fig. 7. Compression curves of tests TH-1 and TV-1.

530 Fig. 8. Tests TH-2, TV-2 and TI: (a) compression curves; (b) hydraulic conductivity curves.

531 Fig. 9. Tests TH-2, TV-2 and TI: (a) hydraulic conductivity versus vertical effective stress; (b)
532 hydraulic conductivity versus void ratio.

533 Fig. 10. Tests TH-2, TV-2 and TI: (a) compression coefficient versus vertical effective stress;
534 (b) consolidation coefficient versus vertical effective stress.

535 Fig. 11. Determination of parameters C_c* and C_α (after Deng et al., 2012).

536 Fig. 12. Tests TH-1 and TV-1: (a) C_c* versus vertical effective stress; (b) C_α versus vertical
537 effective stress.

538 Fig. 13. C_α and C_c* versus vertical effective stress: (a) TH-1; (b) TV-1.

539 Fig. 14. Tests TH-2, TV-2 and TI: (a) C_α versus vertical effective stress; (b) C_c* versus
540 vertical effective stress.

541 Fig. 15. Conceptual representation of the evolutions of C_c* and C_α with vertical effective
542 stress.

543 Fig. 16. C_c* versus C_α.

544 Table 1. Initial characteristics of COx claystone core

Core ID	Density (Mg/m^3)	Dry density (Mg/m^3)	Porosity (%)	Water content (%)	Initial suction (MPa)	Degree of saturation (%)
EST57180	2.4	2.2	17.8	7.8	20.0	97.7

545

546

547 Table 2. Chemical composition of the synthetic water

Components	NaCl	$NaHCO_3$	KCl	$CaSO_4 \cdot 2H_2O$	$MgSO_4 \cdot 7H_2O$	$CaCl_2 \cdot 2H_2O$	Na_2SO_4
Mass (g/L)	0.130	2.216	1.950	0.035	1.082	1.356	0.053

548

549

550 Table 3. Test programme

Test No.	Initial suction (MPa)	Direction of fracture	Thickness of fracture	Core ID	Filter paper	Hydraulic conductivity
TH-1	22.2	Horizontal	0.1 mm	EST57180	yes	no
TV-1	22.6	Vertical	0.3 mm	EST57180	yes	no
TH-2	23.7	Horizontal	0.1 mm	EST57180	no	yes
TV-2	23.3	Vertical	0.3 mm	EST57180	no	yes
TI	22.9	/	/	EST57180	no	yes

551

552

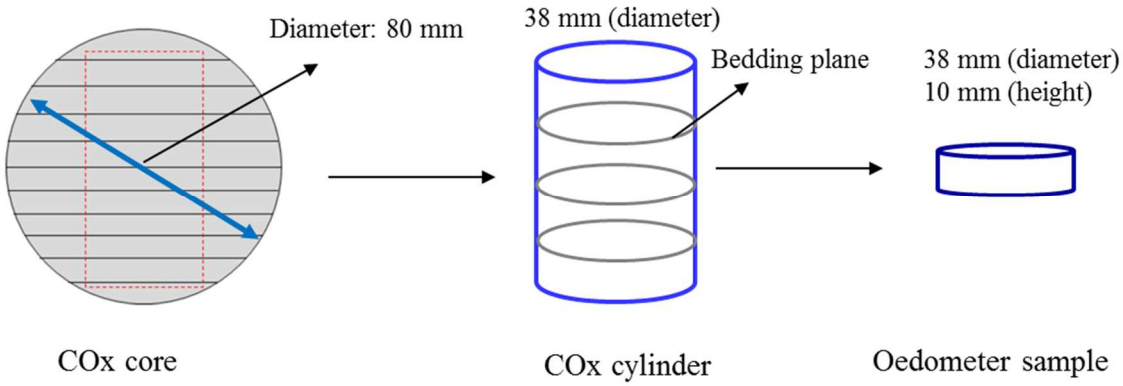

553

554 Fig. 1. Schematic representation of the preparation of intact oedometer samples.

555

556

Fig. 2. Schematic diagram of oedometer samples with horizontally (TH) and vertically (TV) fractured directions and intact sample (TI) (dotted line: fracture).

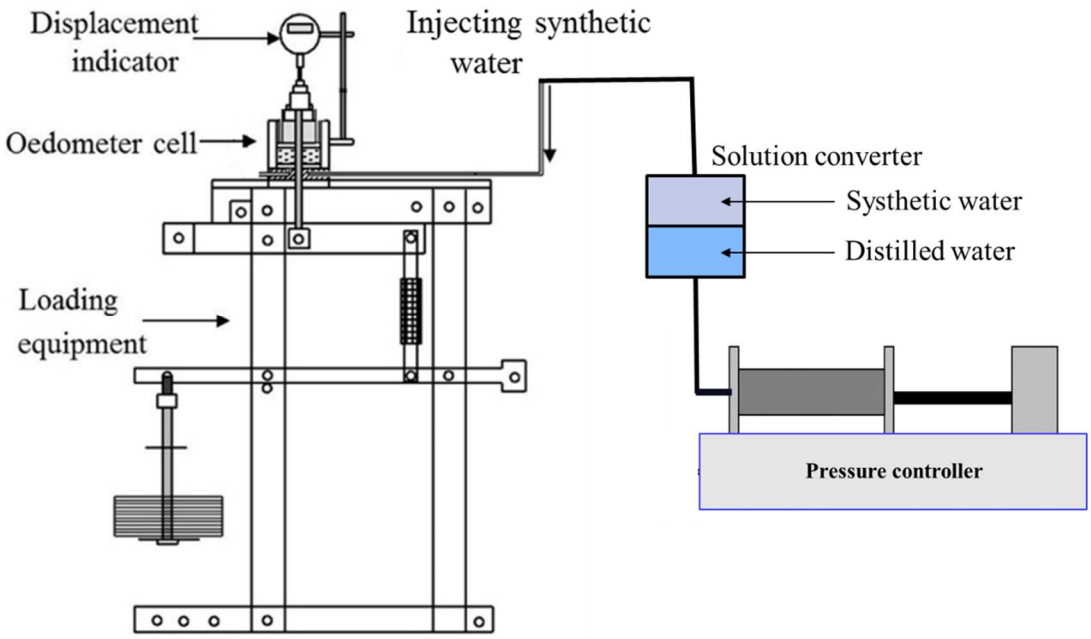

562

563 Fig. 3. High pressure oedometer connected to a pressure-volume controller.

564

565

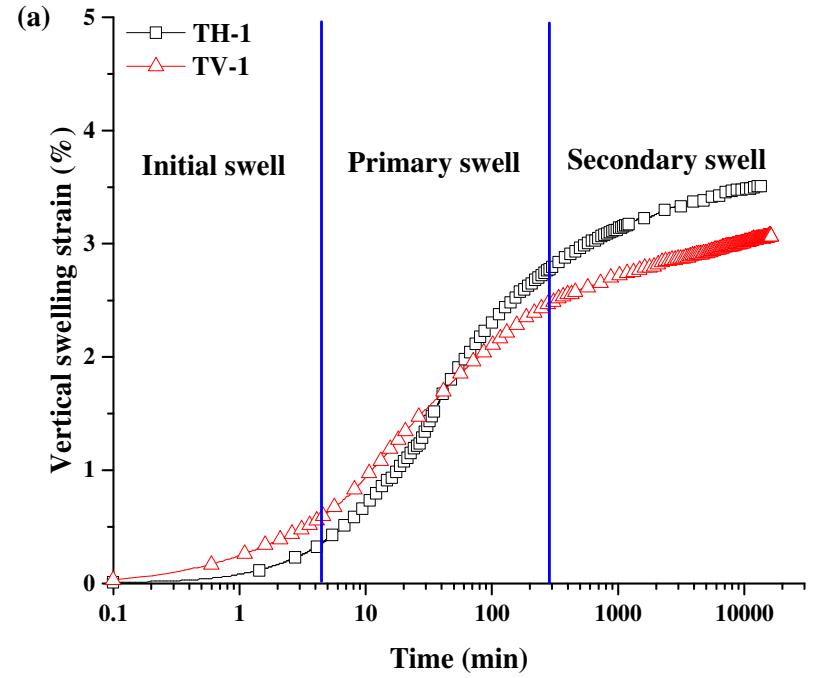

566

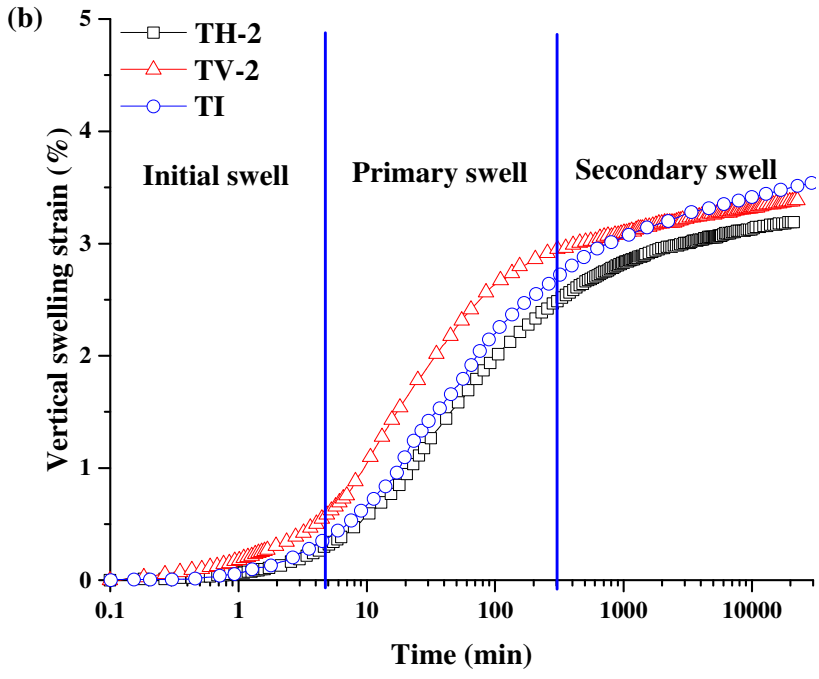

567

568 Fig. 4. Vertical swelling strain versus time; (a) case 1; (b) case 2 and test TI.

569

570

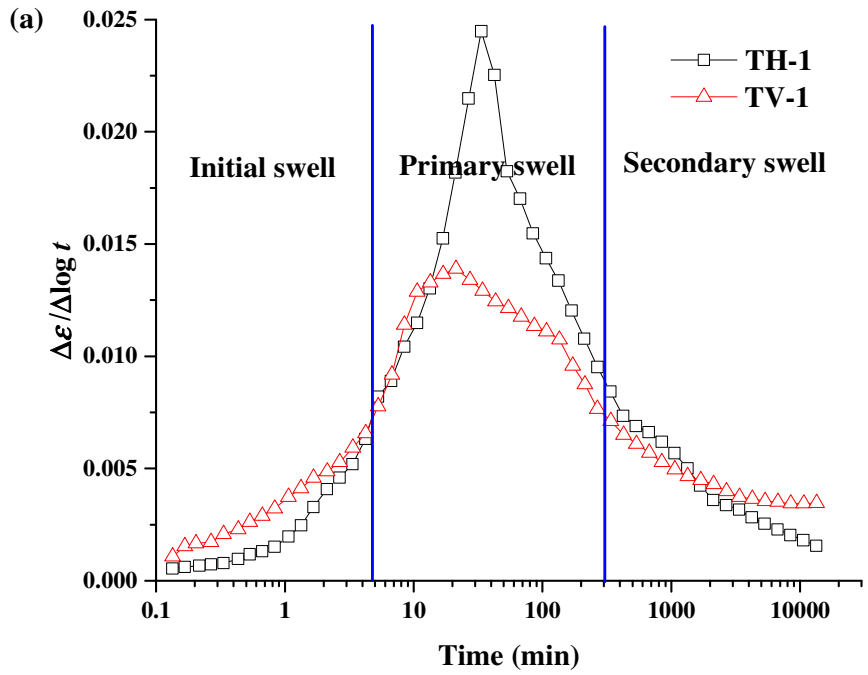

571

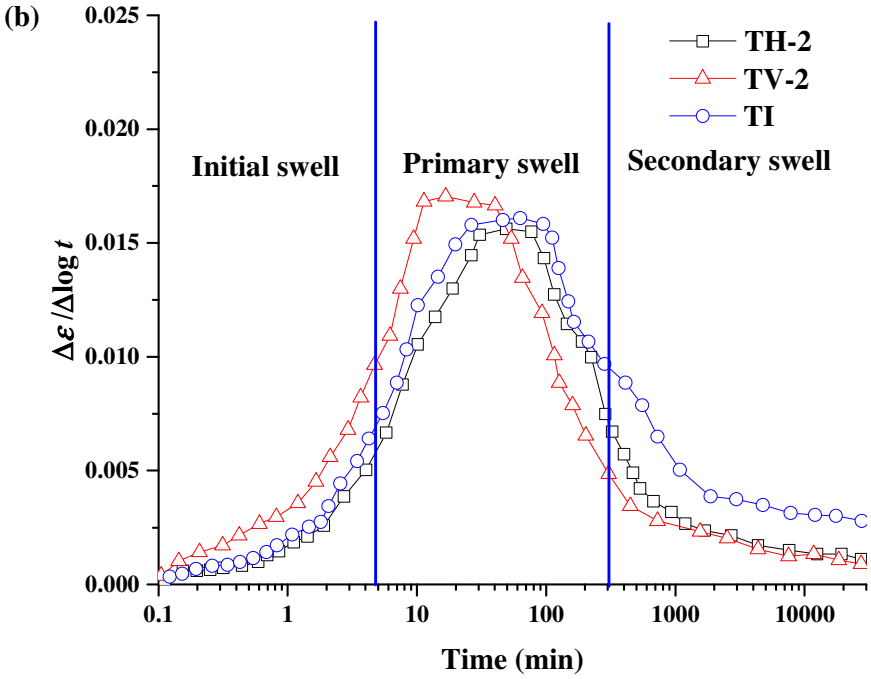

572

573 Fig. 5. Vertical swelling strain rate ($\Delta\varepsilon/\Delta\log t$) versus time: (a) case 1; (b) case 2 and test TI.

574

575

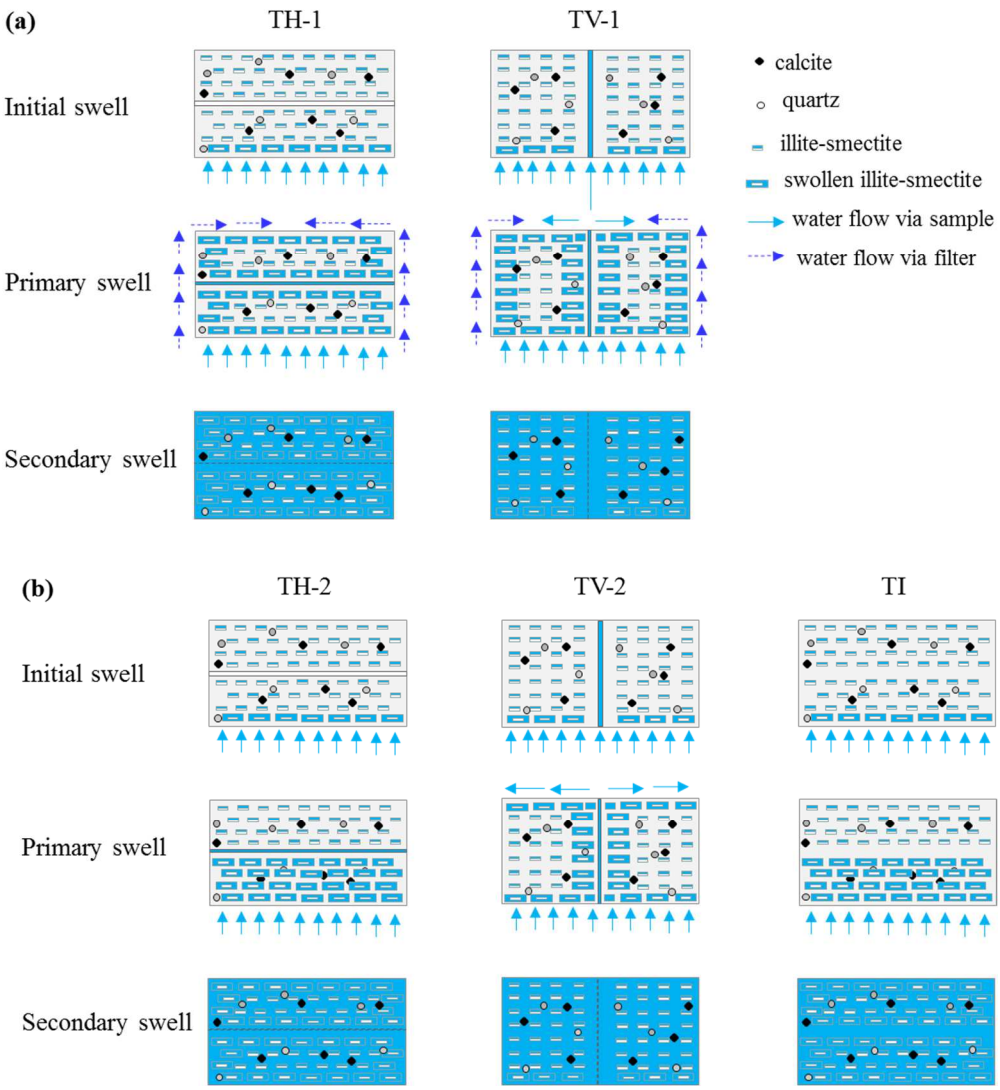

Fig. 6. Schematic view of water infiltration and soil swelling: (a) case 1; (b) case 2 and test TI.

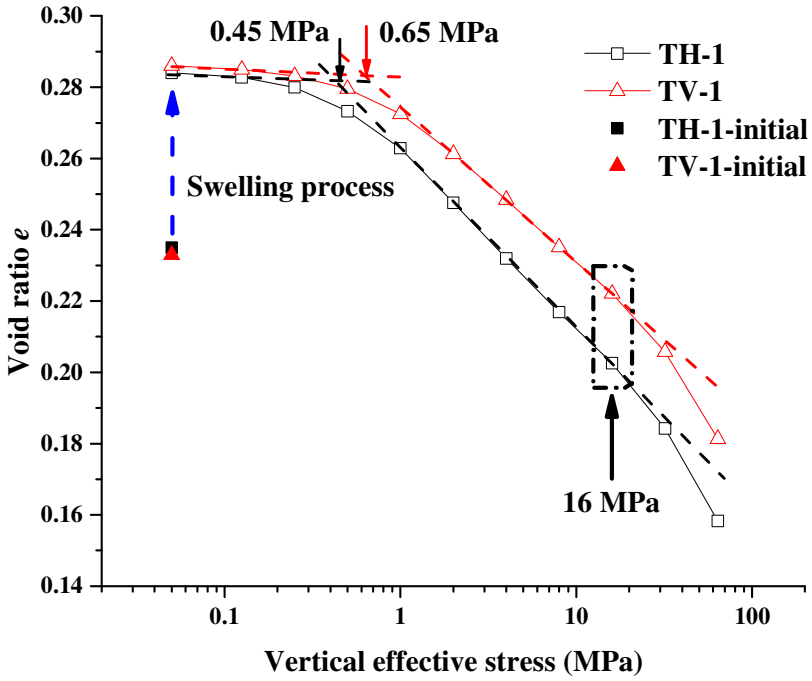

582

583 Fig. 7. Compression curves of tests TH-1 and TV-1.

584

585

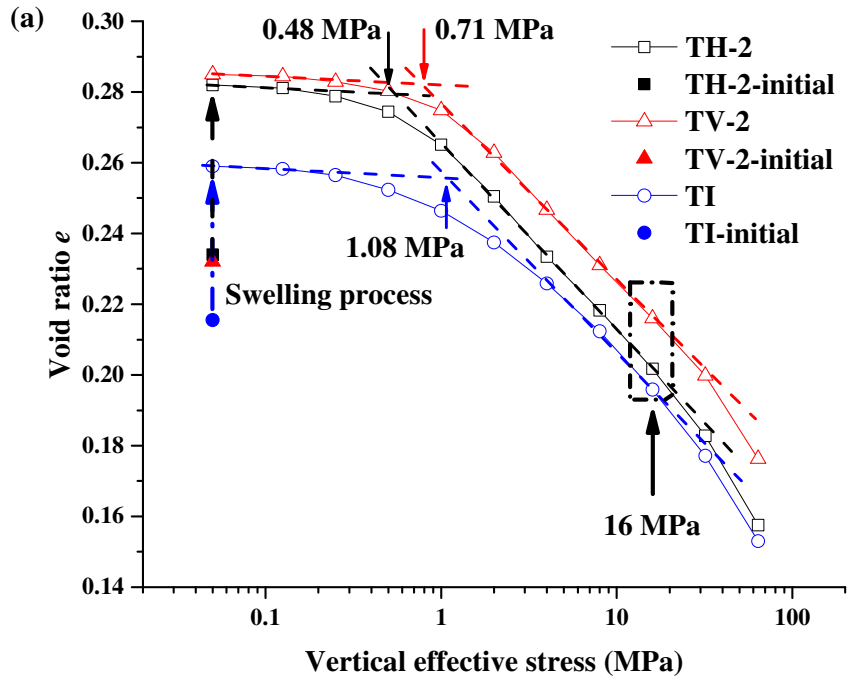

586

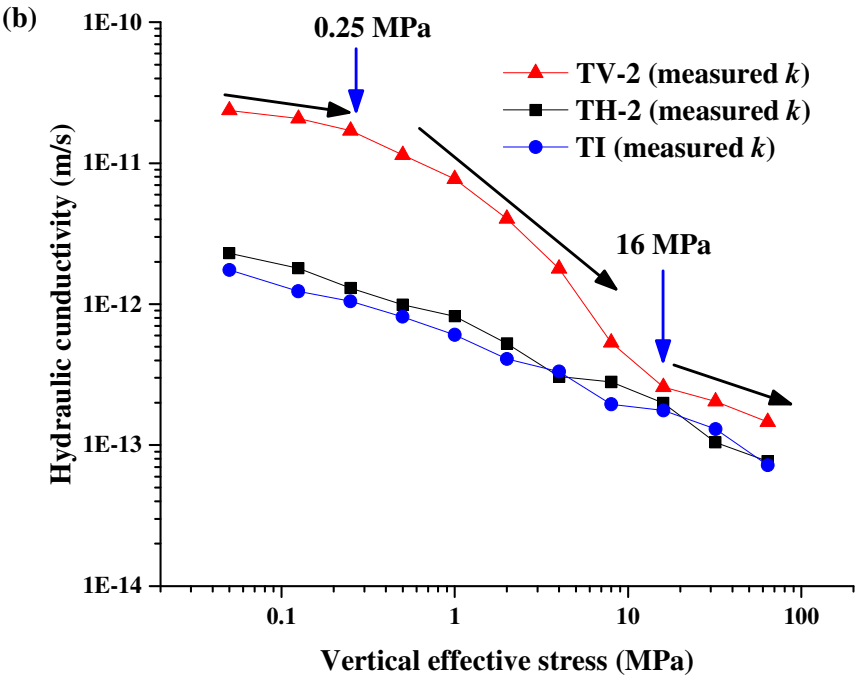

587

588 Fig. 8. Tests TH-2, TV-2 and TI: (a) compression curves; (b) measured hydraulic conductivity

589 curves.

590

591

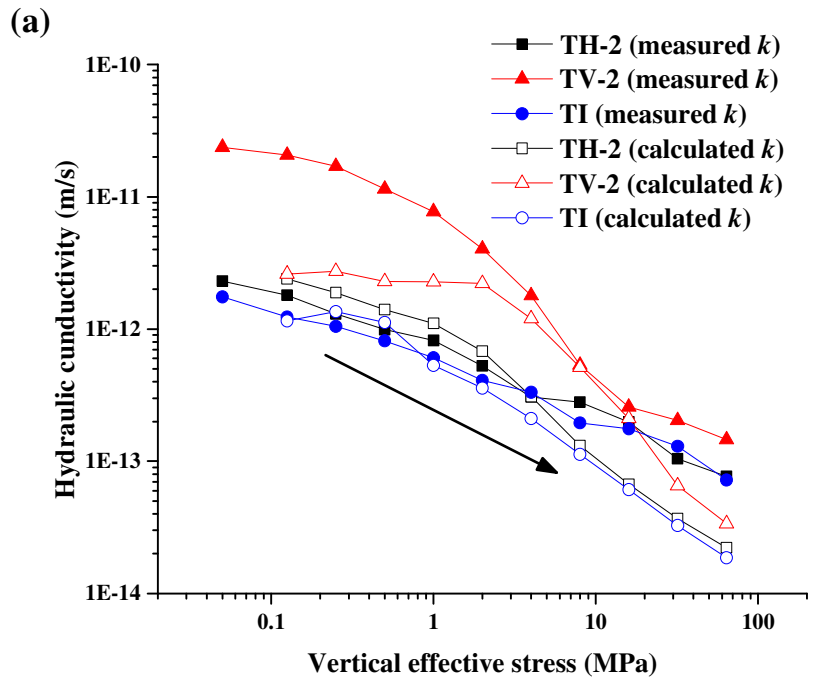

592

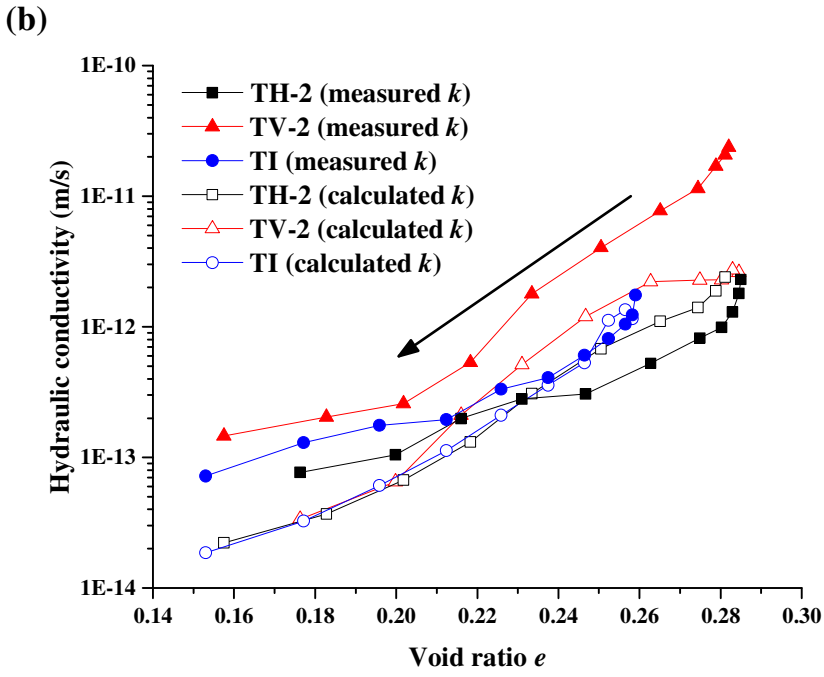

593

594 Fig. 9. Tests TH-2, TV-2 and TI: (a) hydraulic conductivity versus vertical effective stress; (b)

595 hydraulic conductivity versus void ratio.

596

597

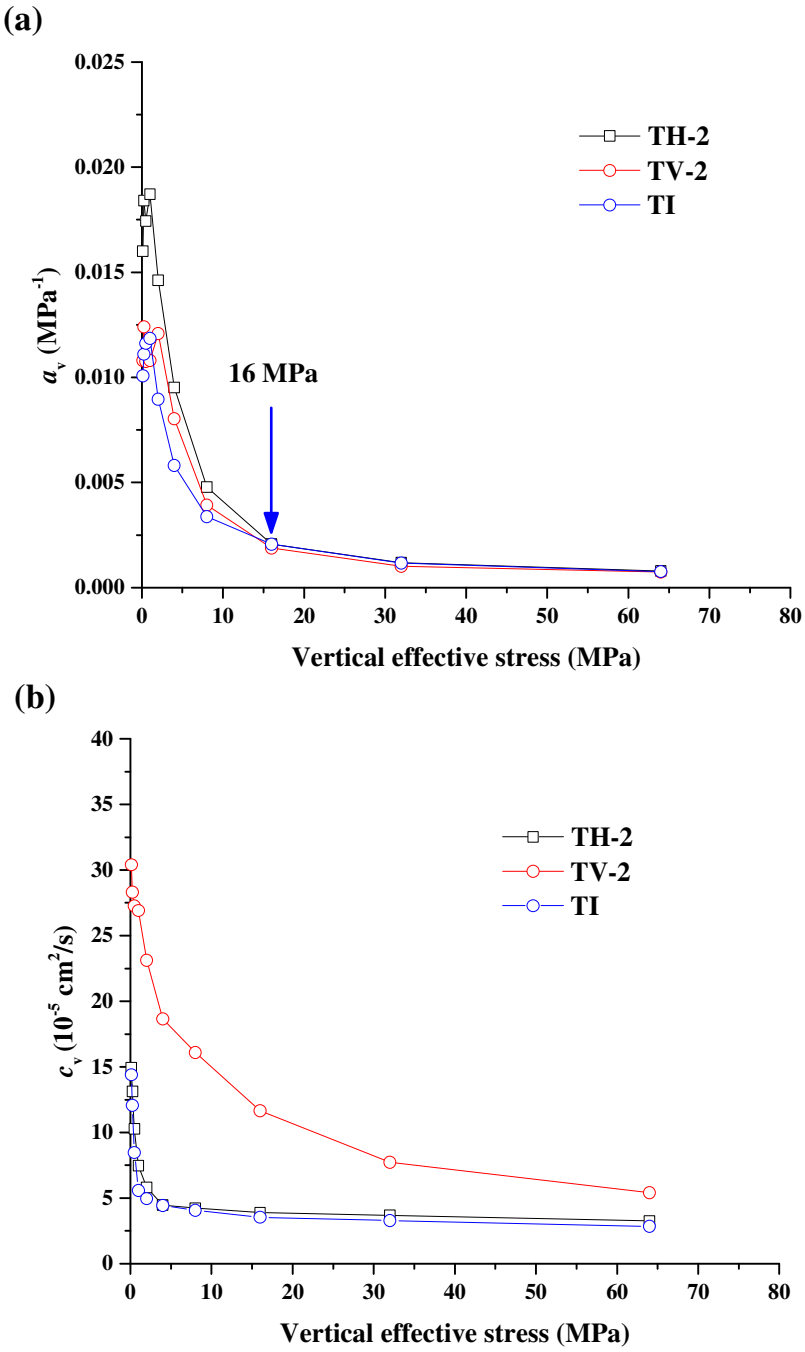

Fig. 10. Tests TH-2, TV-2 and TI: (a) compression coefficient versus vertical effective stress; (b) consolidation coefficient versus vertical effective stress.

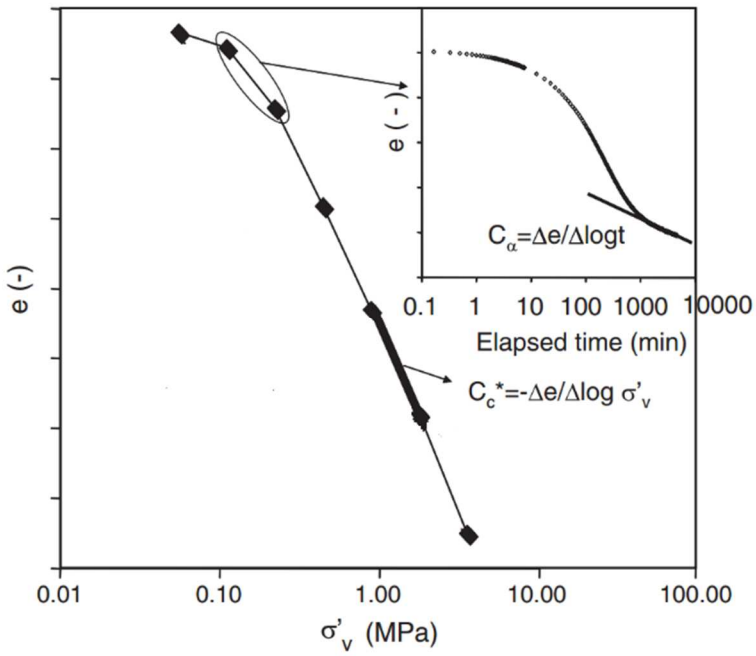

604

605 Fig. 11. Determination of parameters C_c* and C_α (after Deng et al., 2012).

606

607

608

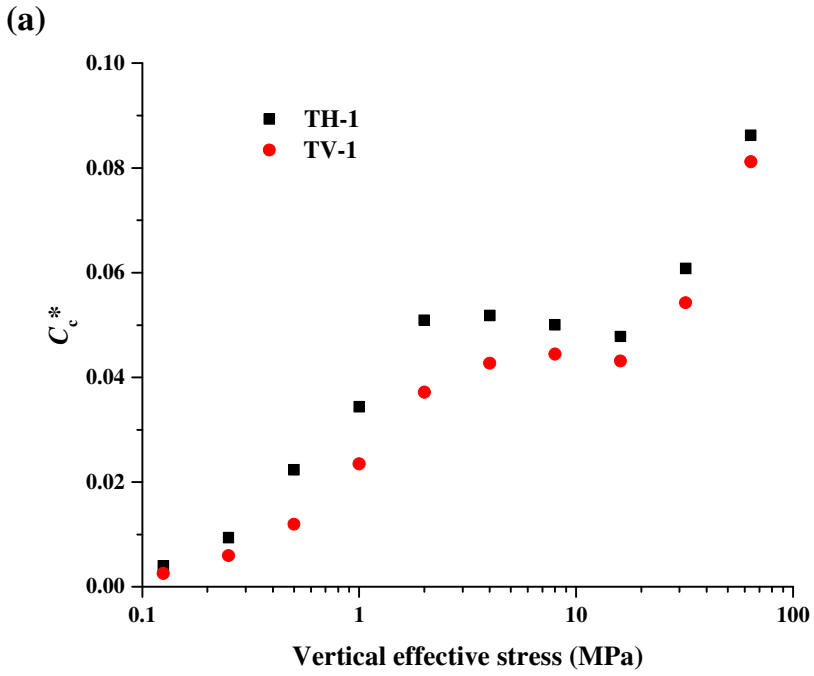

609

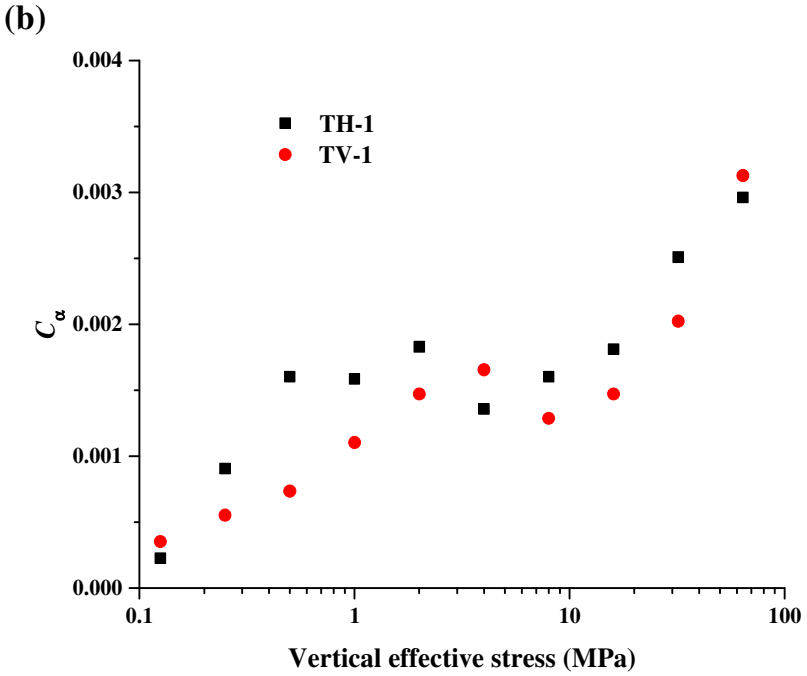

610

611 Fig. 12. Tests TH-1 and TV-1: (a) C_c* versus vertical effective stress; (b) C_α versus vertical

612 effective stress.

613

614

615

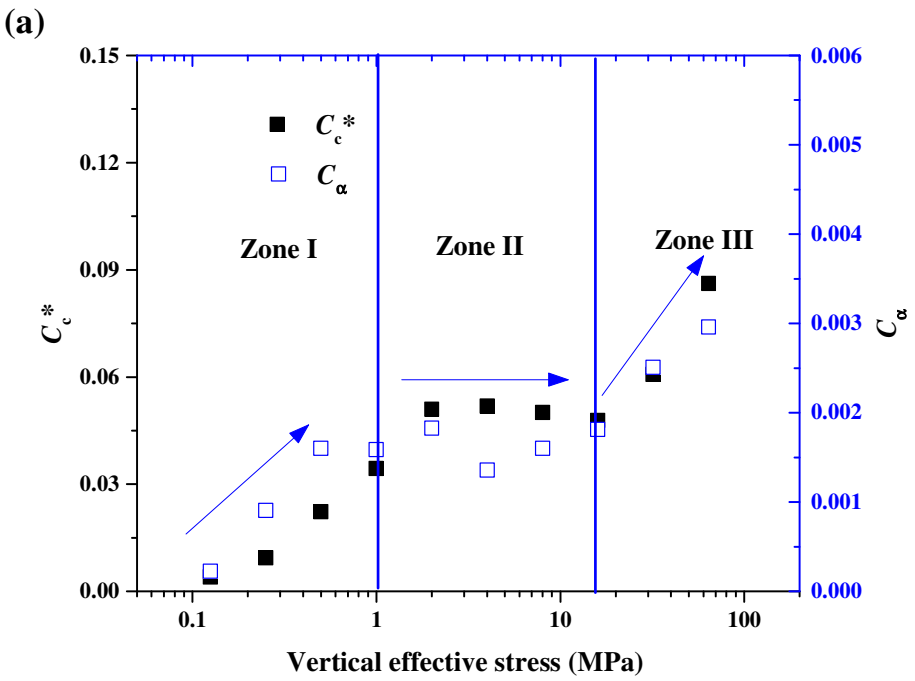

616

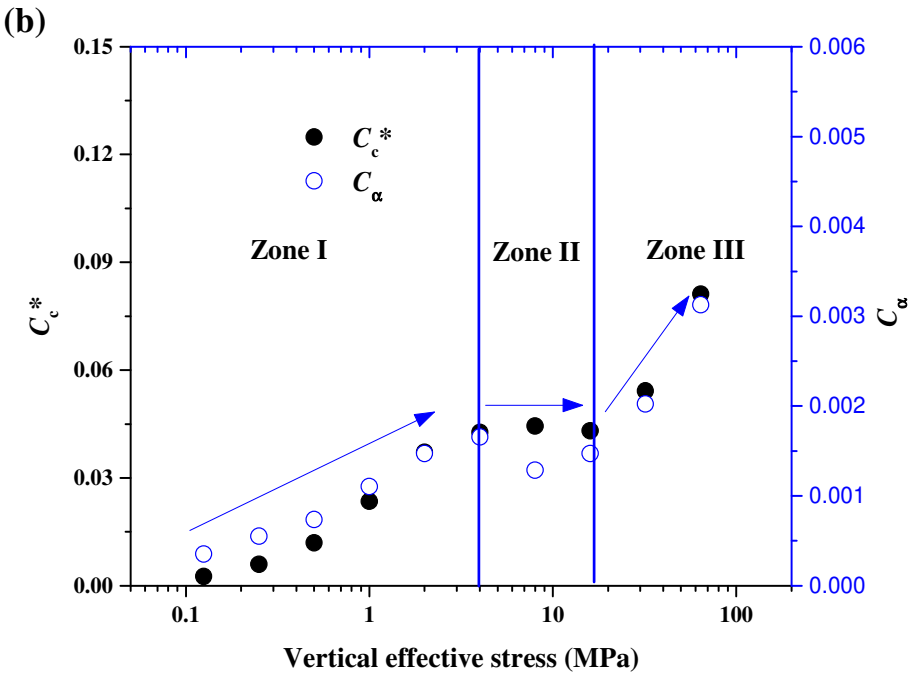

617 Fig. 13. C_α and C_c* versus vertical effective stress: (a) TH-1; (b) TV-1.

618

619

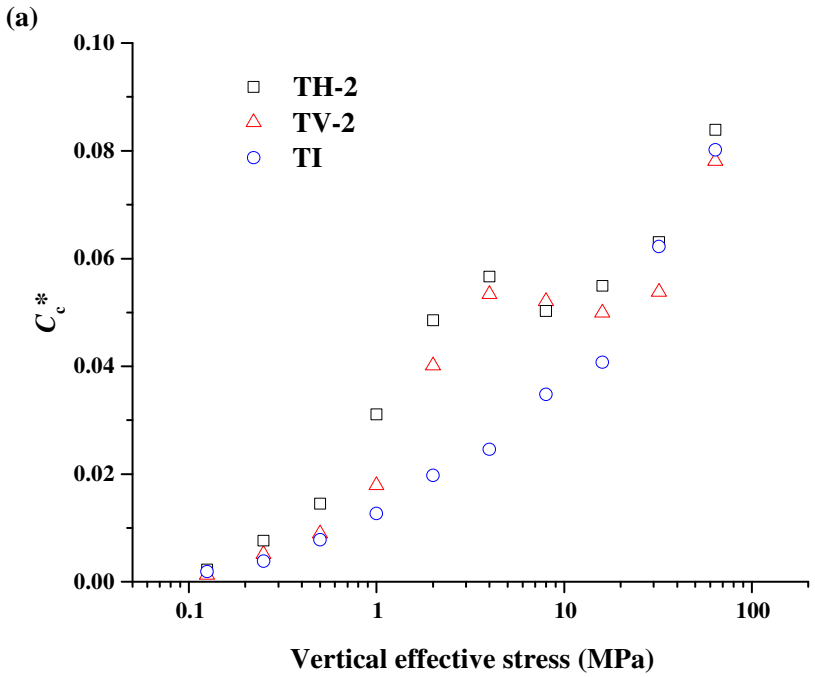

620

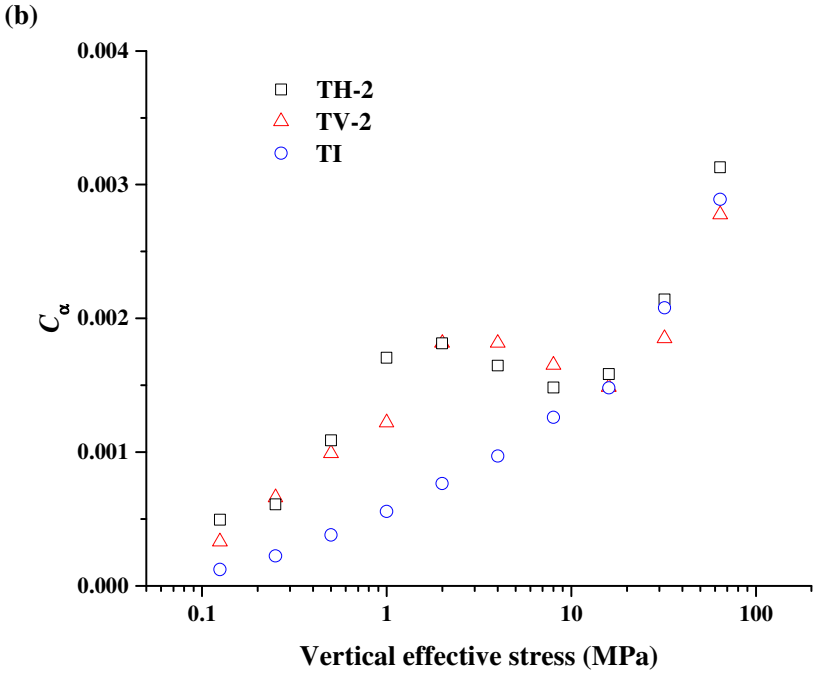

621

622 Fig. 14. Tests TH-2, TV-2 and TI: (a) C_c* versus vertical effective stress; (b) C_α versus

623 vertical effective stress.

624

625

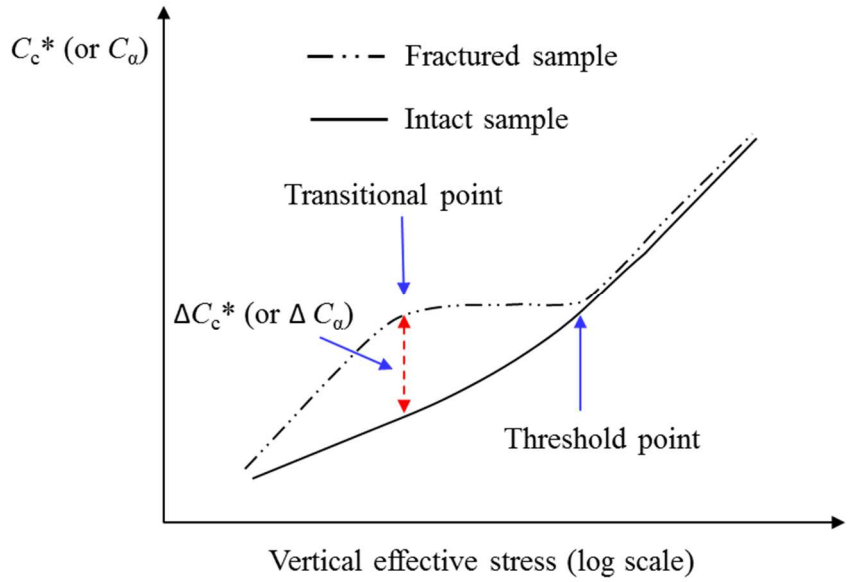

626

627 Fig. 15. Conceptual representation of the evolutions of C_c* and C_α with vertical effective

628 stress.

629

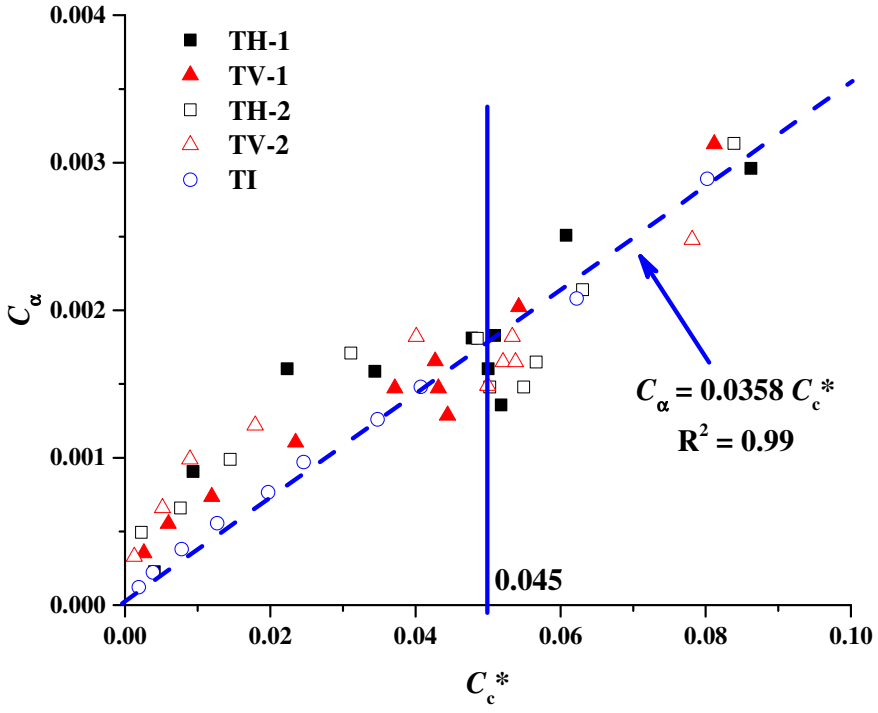

630

631 Fig. 16. C_c* versus C_α.

632